ACS NANO

www.acsnano.org

Hybrid Polymer-Alloy-Fluoride Interphase Enabling Fast Ion Transport Kinetics for Low-Temperature Lithium Metal Batteries

Yuanjian Li,[⊥] Eryang Mao,[⊥] Zhiwen Min,[⊥] Zhao Cai, Zihe Chen, Lin Fu, Xiangrui Duan, Lingyue Wang, Chang Zhang, Ziheng Lu, Wei Liu, Zhi Wei Seh, and Yongming Sun*

Cite This: https://doi.org/10.1021/acsnano.3c08576

Read Online

ACCESS | Metrics & More | Article Recommendations | Supporting Information

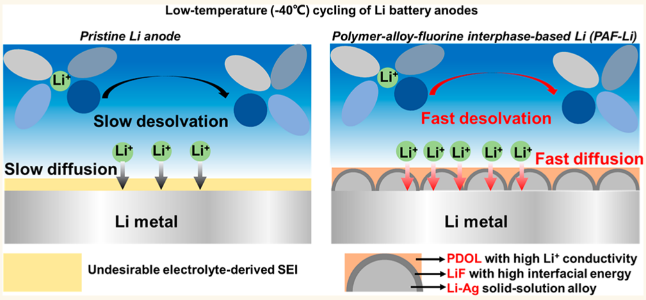

ABSTRACT: **Low-temperature lithium metal batteries are of vital importance for cold-climate condition applications. Their realization, however, is plagued by the extremely sluggish Li^+ transport kinetics in the vicinity of Li metal anode at low temperatures. Different from the widely adopted electrolyte engineering, a functional interphase design concept is proposed in this work to efficiently improve the low-temperature electrochemical reaction kinetics of Li metal anodes. As a proof of concept, we design a hybrid polymer-alloy-fluoride (PAF) interphase featuring numerous gradient fluorinated solid-solution alloy composite nanoparticles embedded in a polymerized dioxolane matrix. Systematic experimental and theoretical investigations demonstrate that the hybrid PAF interphase not only exhibits superior lithiophilicity but also provides abundant ionic conductive pathways for homogeneous and fast Li^+ transport at the Li−electrolyte interface. With enhanced interfacial dynamics of Li-ion migration, the as-designed PAF-Li anode works stably for 720 h with low voltage hysteresis and dendrite-free electrode morphology in symmetric cell configurations at −40 °C. The full cells with PAF-Li anode display a commercial-grade capacity of 4.26 mAh cm^{-2} and high capacity retention of 74.7% after 150 cycles at −20 °C. The rational functional interphase design for accelerating ion-transfer kinetics sheds innovative insights for developing high-areal-capacity and long-lifespan lithium metal batteries at low temperatures.**

KEYWORDS: *lithium metal batteries, low temperature, polymer-alloy-fluoride interphase, fast ion transport, high areal capacity*

The ever-growing demands for highly durable electronic applications in extreme environments (such as high atmosphere, aerospace, polar region, and abysmal sea) necessitate rechargeable batteries with high energy density in all weather conditions, especially at low temperatures (e.g., −20 °C and below).[1−4] Commercial lithium-ion batteries (LIBs) using graphite anodes with low theoretical capacity (372 mAh g^{-1}) are insufficient in terms of energy density (< 300 Wh kg^{-1}) to meet the increasing demand.[5−8] Moreover, graphite anode undergoes dramatically reduced capacity and uncontrolled Li plating behavior when operated at subzero temperatures, making it impractical for low-temperature applications.[9−12] Metallic Li has been pursued as a preferential anode choice for high-energy-density batteries with a wide operating temperature range because of its high theoretical capacity of 3860 mAh g^{-1}, low electrochemical potential of −3.04 V (vs standard hydrogen electrode), and operational electroplating/stripping behavior.[13−16] In recent years, significant progress has been made in enhancing the energy density and extending the lifespan of Li metal batteries (LMBs) at ambient temperatures.[17−20] However, the low-temperature operation of LMBs remains a critical, yet unexplored field.

The primary challenge of low-temperature LMBs is the sluggish and inhomogeneous Li plating/stripping behavior resulting from the undesirable solid electrolyte interphase (SEI) formed by electrolyte decomposition on the surface of lithium metal anode.[21,22] The electrolyte-derived SEI overwhelmingly comprises resistive components, such as Li_2CO_3 and $ROCO_2Li$, giving rise to high energy barriers for Li^+

Received: September 8, 2023
Accepted: September 25, 2023

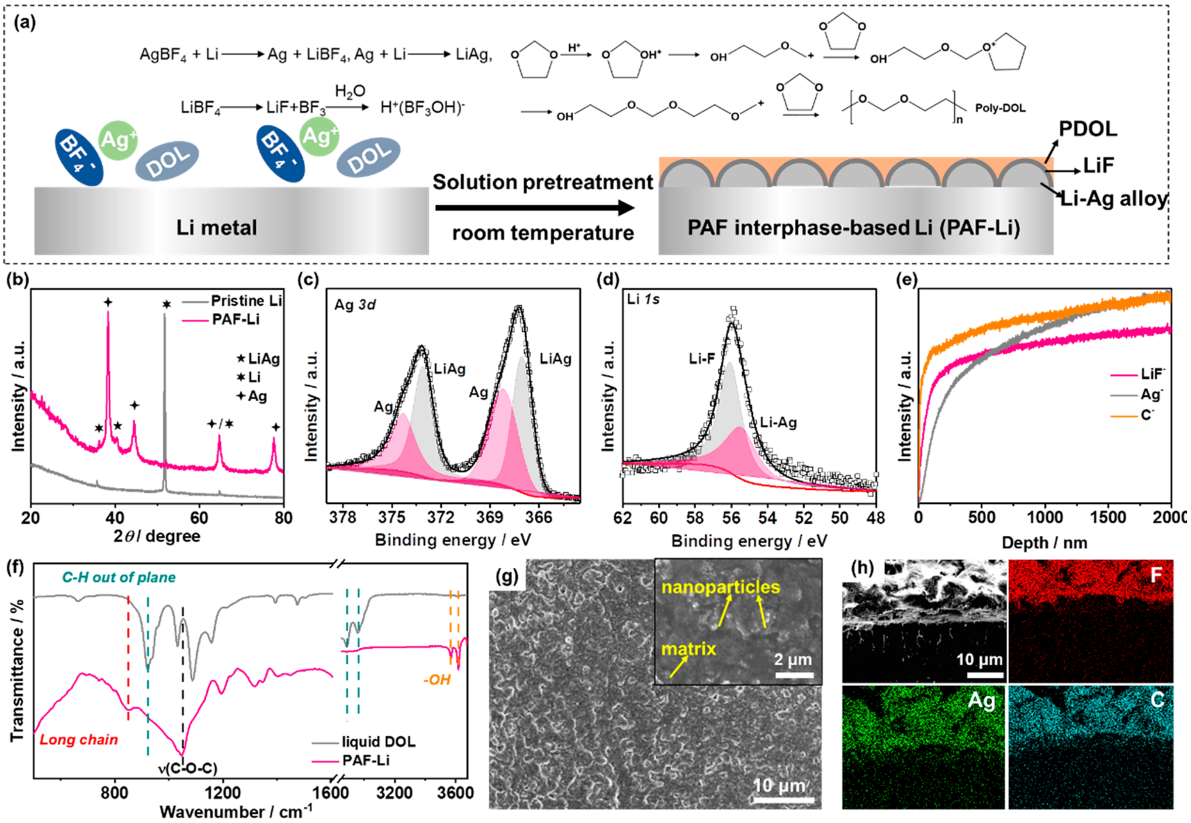

Figure 1. Preparation and characterizations of PAF-Li electrode: (a) fabrication process of PAF-Li metal and reaction mechanism, (b) XRD patterns, high-resolution (c) Ag 3d and (d) Li 1s XPS spectra, (e) TOF-SIMS depth profiles, (f) FTIR spectra, and (g) top-view and (h) cross-sectional SEM images of the PAF-Li metal electrode.

desolvation and transport at the electrolyte/SEI/Li interface and thus spiking cell polarization.[23,24] The as-formed SEI is also known to be fragile and easily ruptured during the dynamic Li plating/stripping process, which would disarrange the distribution of surficial ion flux and further trigger the uncontrollable growth of Li dendrites.[25−27] Accompanied by infinite volume change during cycling, dendritic Li would be converted to electrochemically inactive "dead" Li, ultimately causing premature cell failure and even safety hazards.

To address these issues and build low-temperature Li metal batteries, numerous efforts have been conducted to manipulate electrolyte recipes, such as exploring low-polarizability and low-melting-point solvents to improve low-temperature conductivity,[12,28,29] fluorinating to optimize solvation structure with a low Li^+ desolvation barrier,[30,31] and *in situ* constructing the SEI layers to stabilize the metallic Li surface.[32,33] However, these *in situ* formed SEI layers usually have uncontrolled composition and poor mechanical properties and even continuously consume salts or additives in the electrolytes, causing short lifespan (<500 h) of LMBs at subzero temperatures. Recently, the *ex situ* formation of lithium fluoride (LiF)-rich inner SEI has been proven effective in homogenizing the distribution of ions and stabilizing Li deposition down to −15 °C.[34,35] With low electronic conductivity, large shear modulus (55.1 GPa), and high interface energy (73.28 meV $Å^{-2}$), LiF-rich SEI is also capable of preventing electron tunneling at the Li−electrolyte interface and suppressing dendrite formation.[36−38] However, the poor ionic conductivity (~10^{-12} S cm^{-1}) and high rigidity of LiF[39−41] are undesirable in SEI to ensure sufficient interfacial ionic transfer and withstand electrode volumetric bulge, especially for LMBs working under low-temperature and high-areal-capacity (>4 mAh cm^{-2}) conditions. Therefore, it would be highly desirable, yet challenging, to design an advanced functional interphase, which simultaneously contains fast-ionic conductors, numerous Li^+ transportation pathways, as soft-rigid synergy to realize much enhanced electrochemical kinetics and reversibility in high-areal-capacity and low-temperature Li metal batteries.

Inspired by the above discussion, herein, we design a hybrid polymer-alloy-fluoride interphase featuring numerous gradient Li−Ag/LiF nanoparticles embedded in the polymerized DOL (PDOL) matrix on a metallic lithium surface (PAF-Li) to achieve long-term cycling of high-areal-capacity LMBs under low-temperature conditions. Systematic experimental analyses and theoretical computations demonstrate the compositional and structural merits of the PAF interphase for efficient and stable low-temperature operations of Li metal anode. (1) As the overwhelming polymer matrix in the PAF interphase, PDOL not only exhibits high lithium absorbing ability to facilitate Li^+ desolvation at the Li−electrolyte interface but also acts as a fast-ionic conductor to reduce the energy barrier for lithium transport inside the PAF layer. (2) The homogeneous Li−Ag solid−solution alloy nanoparticles are capable of providing numerous transportation pathways with superior Li-ion diffusivity in the PAF interphase and affording minor phase transformation during repeated lithium plating/stripping. (3) The LiF species that interface with the polymer and alloy components exhibit low Li diffusion barriers and high interfacial energy, which is beneficial for promoting interfacial

https://doi.org/10.1021/acsnano.3c08576
ACS Nano XXXX, XXX, XXX−XXX

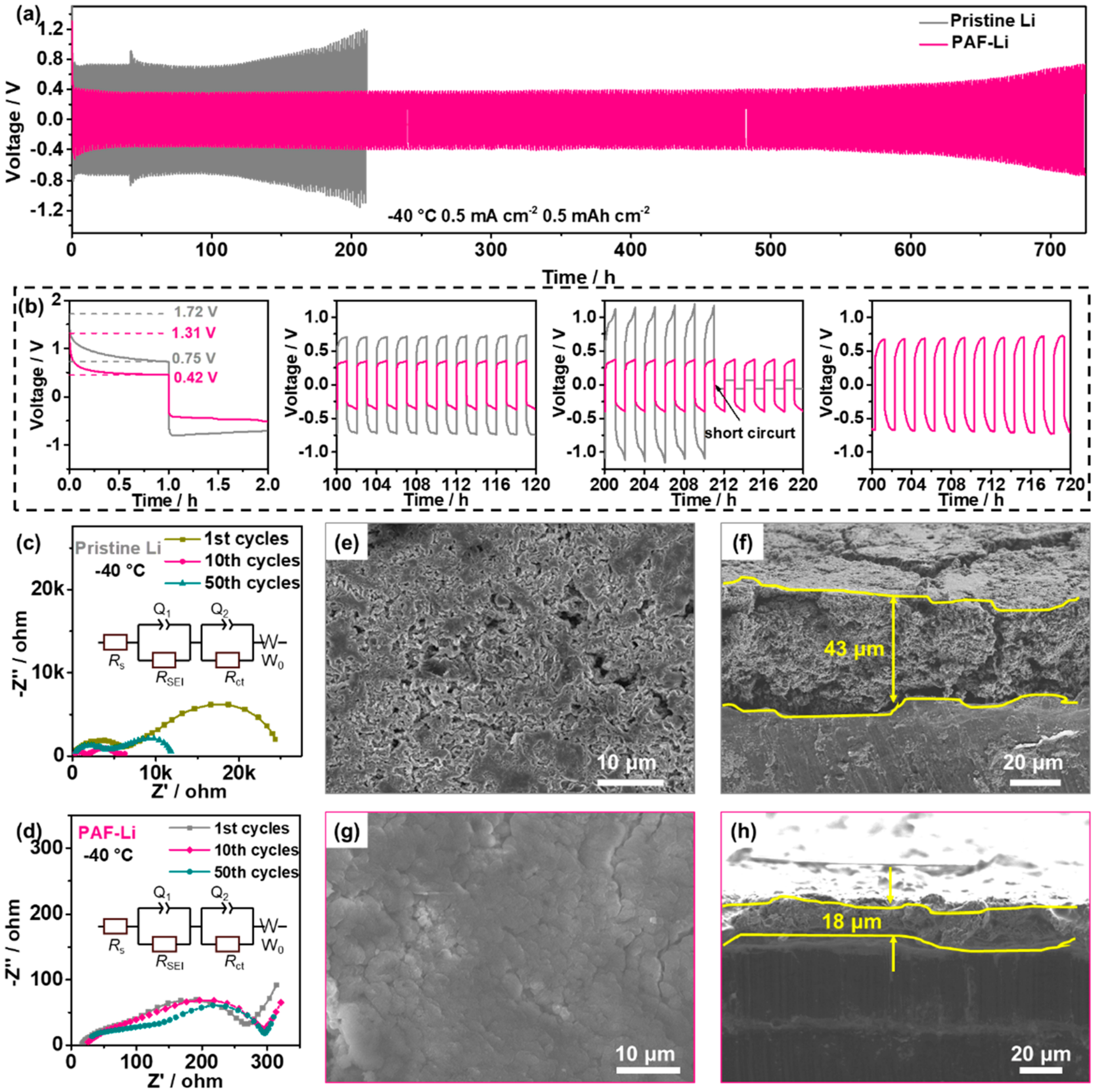

Figure 2. Electrochemical performance of PAF-Li electrodes in symmetric cells at −40 °C. (a, b) Galvanostatic cycling voltage profiles of symmetric cells with pristine Li and PAF-Li electrodes at −40 °C. EIS plots of the symmetric cells with (c) pristine Li and (d) PAF-Li electrodes after different cycles. Top view and cross-sectional SEM images of (e, f) pristine Li and (g, h) PAF-Li electrodes interphase after 50 cycles.

Li^+ transport and suppressing Li dendrite formation. As a result, the obtained PAF-Li anode shows a much longer charging/discharging lifespan (~720 h) with small voltage hysteresis in the symmetric cell cycling at −40 °C than that of the pristine Li metal anode (~200 h). Pairing with a high-loading (5.2 mg cm^{-2}) sulfurized polyacrylonitrile cathode, the PAF-Li based full cell exhibits an industrial-level areal capacity of 4.26 mAh cm^{-2} at −20 °C and high cycling stability over 50 cycles at −40 °C, demonstrating great promise for high-areal-capacity and temperature-tolerant LMBs.

RESULTS AND DISCUSSION

Preparation and Characterization of PAF-Li Metal. Figure 1a schematically illustrates the fabrication process of a polymer-alloy-fluoride interphase-based Li metal electrode (PAF-Li) and the reaction mechanism. By dropping an $AgBF_4$-DOL solution on the Li metal surface, a high-energy replacement reaction takes place ($Li + AgBF_4 \rightarrow Ag + LiBF_4$, $\Delta H_{calculated} = -406$ kJ mol^{-1}). The displaced metallic Ag can react with the underlying lithium to form a Li−Ag alloy due to their significant difference in Fermi energy levels.[42−44] Moreover, the Li−Ag phase diagram also verifies that the β-phase LiAg alloy is the thermodynamically stable phase (Figures S1 and S2). At the same time, the $LiBF_4$ product is prone to produce LiF and strong Lewis acid BF_3, the latter of which can act as an "initiator reservoir" in the presence of trace water (~20 ppm) in the solvent to trigger the ring-opening polymerization of the DOL solvent via the cationic mechanism.[33,45,46] After drying in the Ar-filled glovebox, the pristine Li foil turns from shiny silver to black, demonstrating the formation of a hybrid layer after the reaction (Figure S3). Because of its sensitivity to air, pristine Li metal is corroded quickly, and its color becomes gray after 3 h of exposure to air (Figure S4). Interestingly, there is almost no noticeable color change for PAF-Li under the same test condition. Such high air stability of PAF-Li (Figure S5) is highly desirable for practical applications in Li-metal battery systems.

X-ray diffraction (XRD) and X-ray photoelectron spectroscopy (XPS) measurements were conducted to characterize the surface compositions of PAF-Li metal electrodes. As depicted in Figure 1b, typical XRD peaks of metallic Li (PDF no. 15-0401) at 36.2°, 52.4°, and 65.1° can be detected for both pristine Li and PAF-Li electrodes. Apart from the above peaks, the PAF-Li also exhibits peaks at 38.1°, 40.2°, 44.3°, 64.5°, and 77.5°, which are indexed to metallic Ag (PDF no. 04-0783) and LiAg alloy (PDF no. 04-0805). The phase diagram reveals a large region of Ag-rich solid solution (Li "dissolved" in Ag, the α-phase) before the formation of the β-phase LiAg alloy.[42−44] Thus, the metallic Ag peaks are the reflection of the α-phase Ag-rich solid solution rather than elemental Ag. The high-resolution Ag 3d XPS spectrum (Figure 1c) further supports the coexistence of Ag and Li−Ag in the hybrid layer of PAF-Li, which can act as a mixed electronic/ionic conductor to accelerate charge transport. Figure 1d shows the high-resolution Li 1s XPS spectrum, where one peak at 55.5 eV is further evidence of the formation of Li−Ag alloy and another at 56.0 eV assigned to the Li−F bond appears, demonstrating the formation of LiF. In the high-resolution C 1s spectrum (Figure S6), three deconvoluted peaks at 284.8, 286.8, and 288.1 eV can be assigned to the C−C/C−H, C−O−R, and −COOR groups of polyether.[47,48] Time-of-flight secondary ion mass spectrometry (TOF-SIMS) tests were performed to investigate the spatial distribution of the Li−Ag alloy, LiF, and C species in the PAF interphase. As shown in Figure 3e, the signal intensity of Ag^- gradually exceeds that of LiF^- with increasing sputtering depth, indicating that Li−Ag alloy and LiF are mainly distributed at inside and outside the PAF interphase, respectively. The relatively high intensity of C^- signal during the whole sputtering process suggests that the polymer phase serves as an overwhelming matrix in the PAF interphase. To further clarify the polymer phase in PAF-Li, Fourier transform infrared spectroscopy (FTIR) technology was employed. Compared with pure DOL solvent, the FTIR spectrum of PAF-Li (Figure 1f) displays the appearance of vibration models related to long-chain species (red) and C−OH (orange), the virtual disappearance of the C−H out-of-plane vibration (dark cyan), and the displacement of the C−O−C vibration (black) from 1030 to 1000 cm^{-1}. These distinct changes in FTIR spectra agree well with previous reports[47,48] and strongly indicate the existence of the PDOL phase in PAF-Li.

The morphological features of the PAF-Li metal electrode were investigated by scanning electron microscopy (SEM). Compared with the pristine Li electrode (Figure S7), the PAF-Li displays a relatively rough surface with numerous nanoparticles embedded in a compact matrix (Figure 1g). The thickness of the PAF layer reaches approximately 12 μm (Figure 1h), accounting for only ~4% volume of a 300 μm lithium foil used in this work, and is comparable to advanced artificial protective layers in recent reports.[15] The surface and cross-sectional energy dispersive X-ray (EDX) maps (Figures 2h and S8) validate the uniform distribution of the Ag, F, and C elements in the hybrid PAF layer. Such a microstructure of PAF-Li ensures sufficient charge transfer pathways, reduces local current density, diminishes significant volume change, and restrains undesired side reactions during long-term cycling. We also conducted control experiments by treating Li metal with a $LiBF_4$ (lithium tetrafluoroborate)-DOL solution or $AgBF_4$-DME (1,2-dimethoxyethane) solution. The corresponding characterizations (Figures S9 and S10) indicate that $LiBF_4$-DOL treated Li has a compact PDOL layer, whereas $AgBF_4$-DME treated Li possesses a porous Li−Ag/LiF layer only. Although the compact PDOL layer can isolate the active Li metal from liquid electrolytes, the retarded interfacial reactions would give rise to a large overpotential during the Li plating/stripping process (Figure S11). The porous Li−Ag/LiF layer with a large electrolyte-accessible surface area may improve Li transfer; however, unavoidable interfacial side reactions would shorten the lifespan of batteries (Figure S12).

Advantages of PAF Interphase for Fast Low-Temperature Reaction Kinetics. With the successful synthesis of the PAF hybrid layer, we then investigated its modulation effect on the electrochemical behavior of Li-metal anodes at low temperatures. 1 M lithium bis(trifluoromethanesulfonyl)imide (LiTFSI) in DOL:DME:fluoroethylene carbonate (FEC) = 5:5:1 vol % was chosen as the electrolyte since it showed a satisfactory ionic conductivity at low temperatures.[10] Figure 2a and Figure 2b show typical voltage profiles of symmetric cells with pristine Li and PAF-Li electrodes tested at −40 °C at 0.5 mA cm^{-2} and 0.5 mAh cm^{-2}. We found that a large overpotential of 1.72 V is required to initiate pristine Li cell charging. The overpotential is reduced to 0.75 V at the end of the first charging process and remains stable during the following 100 h cycling. When the cycling was continued, the overpotential gradually increased to about 1.12 V after 200 h, which is associated with severe electrode degradation. A sudden voltage drop emerged at 212 h, suggesting a short circuit of the pristine Li symmetric cell that is caused by the growth and accumulation of dendritic Li. In contrast, the as-designed PAF-Li||PAF-Li symmetric cell exhibited a relatively small overpotential of 1.31 V during the initial charging process. The voltage hysteresis remained as low as ~0.50 V in the following charge/discharge cycling (~720 h). It is also worth noting that the cumulative cycling capacity (~360 mAh cm^{-2}) of our PAF-Li anode at a low temperature of −40 °C outperformed those reported low-temperature Li metal symmetric cells so far (Table S1).[23,25,49] When operated at room temperature, the PAF hybrid layer also endowed the metallic Li anodes with a prolonged lifespan at a high current density of 10 mA cm^{-2} (250 h, Figures S13 and S14) and under a deep cycling capacity of 10 mAh cm^{-2} (400 h, Figures S15 and S16). These values compare favorably with the pristine Li electrode and other modified Li metal anodes in literature cycling at room temperature (Table S2). The wide range of temperatures, high-current, and large-capacity applied to our PAF-Li anodes hold great promise to meet the requirements in practical applications.

The electrochemical impedance spectra (EIS) of symmetric cells with pristine Li and PAF-Li electrodes after different low-temperature cycles are recorded in Figure 2c,d. By fitting into the equivalent circuit, R_{SEI} (resistance of Li^+ diffusion through the SEI) and R_{ct} (resistance of charge transfer at the electrolyte-anode interface) can be deconvoluted from high-frequency and low-frequency semicircles in Nyquist plots, respectively. As summarized in Table S3, PAF-Li metal electrode depicts 2 orders of magnitude lower values of R_{SEI} than those of pristine Li electrode, suggesting that the artificial hybrid interphase on PAF-Li metal enables faster Li ionic transmission than the native SEI on pristine Li electrode.[50,51] Simultaneously, the R_{ct} values are also seen to experience a

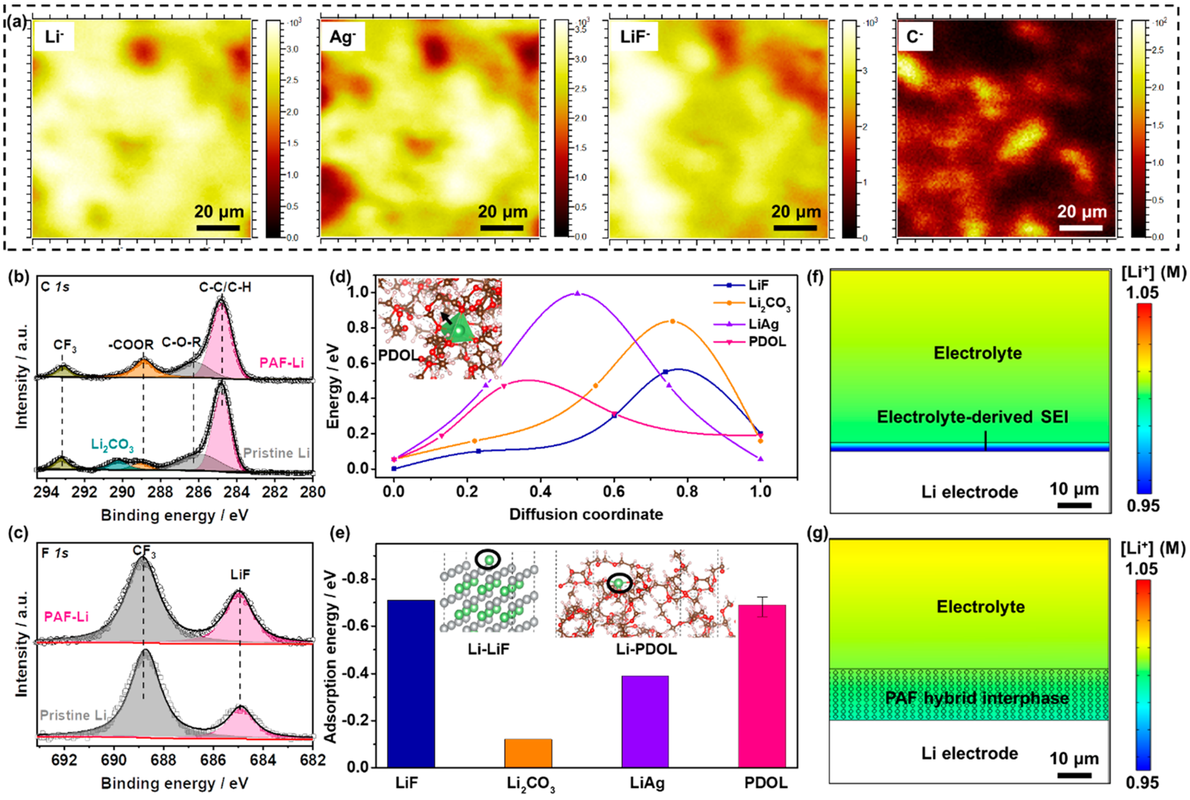

Figure 3. Kinetics advantages of PAF-Li for low-temperature operation. (a) TOF-SIMS color mappings of Li^-, Ag^-, LiF^-, and C^- fragments and high-resolution (b) C 1s and (c) F 1s XPS spectra for PAF-Li electrodes after cycling at −40 °C. (d) Summary of the calculated Li ion diffusion barriers in in LiF, Li_2CO_3, LiAg, and PDOL. Inset: the modeling of Li diffusion paths in DOL. The black arrow indicates the Li ion diffusion direction. (e) Summary of the calculated adsorption energies of Li atom on LiF, Li_2CO_3, LiAg, and PDOL. Inset: Adsorption configurations of Li atom on LiF and PDOL. Here, the green, gray, brown, and red balls represent Li, F, C, and O elements, respectively. COMSOL simulations of the Li^+ flux distribution on the surface of Li metal anode with (f) electrolyte-derived Li_2CO_3 rich SEI and (g) PAF hybrid interphase. The simulation was conducted at 0.5 mA cm^{-2} with a low temperature of −40 °C.

nearly 10-fold decrease by replacing pristine Li with PAF-Li metal electrode, which ascribed to the high "lithiophilicity" of PDOL, Li−Ag solid solution, and LiF on the surface of PAF-Li that affords high affinity to Li atoms and favorable charge transfer capability. The interfacial movement of Li ions was further evaluated by the exchange current density (j_0) derived from the Tafel plots. As displayed in Figure S17, the calculated j_0 of the PAF-Li electrode reaches 75.1 μA cm^{-2}, much higher than that of the pristine Li counterpart (2.1 μA cm^{-2}), further ascertaining that the polymer-alloy-fluoride layer is highly conducive to facilitating Li-ion transport at the electrolyte/Li interface. From the Nyquist plots, it is also noteworthy that the resistance of the PAF-Li symmetric cell remains nearly constant throughout the cycling, verifying that the hybrid PAF interphase can stabilize the electrolyte−anode interface, which accounts for the stable battery cycling performance as observed in Figure 2a,b. For pristine Li symmetrical cell, the resistance becomes lower in the first 10 cycles, which is related to the exposure of active lithium resulting from repeated breakdown/repair of the native SEI.[27] The consumption of active lithium and electrolyte along with the accumulation of dendrites impeded the Li-ion transport, leading to the increase of cell resistances after 50 cycles and rapid cell failure.

Post-mortem SEM observations were further conducted to corroborate the electrochemical behavior of the pristine Li and PAF-Li electrodes. The SEM image of pristine Li electrode after 50 cycles (Figure 2e) illustrates a coarse surface with large and irregular cavities, indicating nonuniform Li deposition and uncontrolled growth of Li dendrites. The random Li plating/stripping behavior also triggered a thick porous "dead" lithium layer (~43 μm) generated on the pristine Li electrode (Figure 2f). In contrast, an extraordinarily dense surface without obvious dendritic or mossy Li can be observed on the cycled PAF-Li anode surface (Figure 2g). As exhibited in the cross-sectional SEM image (Figure 2h), the thickness of the PAF layer increased from 12 to 18 μm, and the close contact between the PAF layer and the underlying metallic Li is maintained after 50 low-temperature cycles. These SEM observations suggest the superiority of hybrid PAF layer in stabilizing the electrolyte−electrode interface and in keeping electrode integrity during continues low-temperature plating and stripping.

To probe the surface chemistry of the PAF-Li metal electrode after cycling at −40 °C, TOF-SIMS and XPS measurements were performed. As depicted in Figures 3a and S18, the TOF-SIMS surface color mappings and 3D reconstructed images demonstrate that the hybrid PAF interphase contains a uniform distribution of Li^-, Ag^-, and LiF^-, and C^- fragments on the surface of cycled PAF-Li electrode. The XPS results further indicate that the surface composition of the PAF-Li does not change significantly before and after the low-temperature cycling, except for the emergence of CF_3 species arising from the decomposition of LiTFSI (Figures 3b,c and S19). For the cycled pristine Li electrode, typical electrolyte-derived products, including Li_2CO_3 (290.2 eV), COOR (289.0 eV), and C-OR (286.0

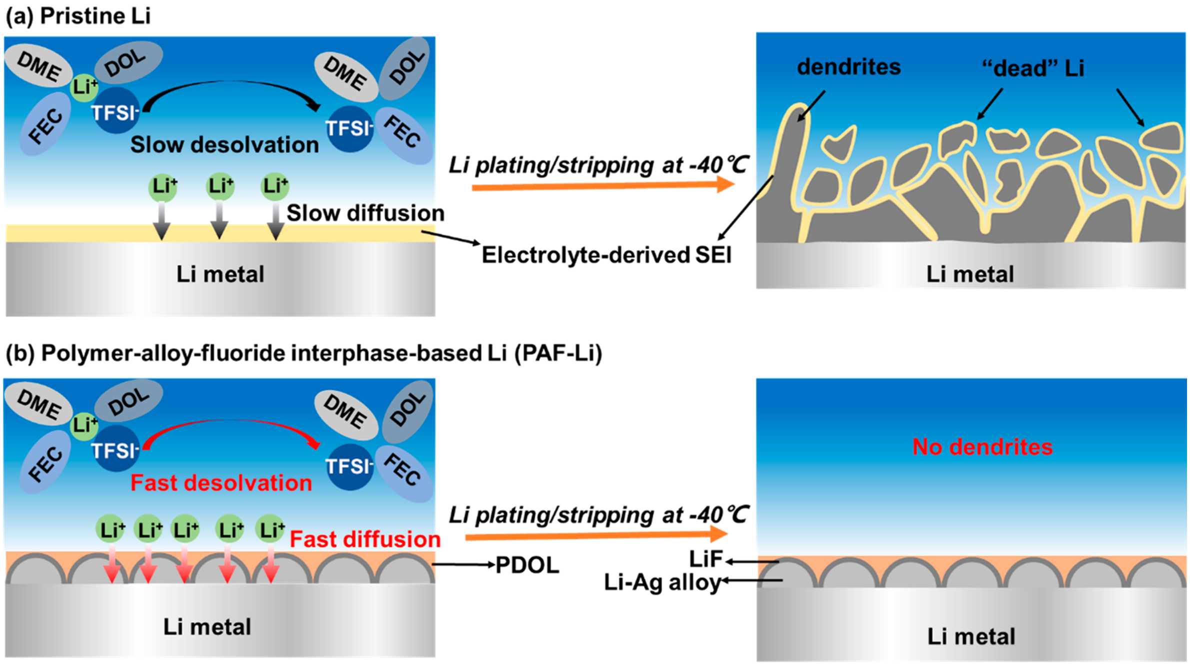

Figure 4. Schematic for Li metal anodes working at a low temperature of −40 °C. (a) Pristine Li metal electrode. It suffers sluggish Li-ion transport kinetics and uncontrolled formation of Li dendrites, which are the key challenges in low-temperature Li metal batteries. (b) Polymer-alloy-fluoride interphase-based Li metal electrode (PAF-Li). The synergistic effects of PDOL, Li−Ag solid−solution alloy, and LiF in the PAF endow the Li metal anode with fast and uniform Li-ion transport capability as well as dendrite-free lithium plating/stripping behavior at −40 °C.

eV) in the C 1s spectrum (Figure 3b) and LiF (685.9 eV) in the F 1s spectrum (Figure 3c), appear on its surface. These results agree well with the composition found in the previous SEI characterization.[14] Compared to that of the pristine Li electrode, the relative ratio of CF_3 to LiF on the PAF-Li electrode is significantly lower, demonstrating that PAF hybrid interphases can effectively reduce electrolyte decomposition during repeated cycling. The relatively high content of LiF species, with low diffusion energy barrier (0.57 eV, Figure S20) and high surface energy (73.28 meV $Å^{-2}$), is capable of endowing sufficiently fast Li-ion mobility in the PAF interphase. The formation of Li_2CO_3, which exhibits high surface diffusion energy (0.75 eV, Figure S21) and low interfacial energy (59.22 meV $Å^{-2}$), is eliminated on the surface of the PAF-Li electrode. This phenomenon provides further evidence of the effectiveness of the hybrid polymer-alloy-fluoride interphase in reducing the barriers for Li-ion transport within the PAF-Li electrode during low-temperature operations.

To elucidate the mechanism of superior Li-ion migration on the interfacial layer of the PAF-Li anode, density functional theory (DFT) calculations were employed. According to the computational results (Figures 4d and S20), the diffusion energy barrier of Li ions on the Li−Ag surface reaches 0.90 eV, while that on a PDOL surface is only 0.41 eV. These results are consistent with previous molecular dynamics simulations that the PDOL phase favors a high Li−O coordination number and superior ionic conductivity (1.4×10^{-5} S cm^{-1} at −20 °C), thereby functioning as ionic channels to boost Li^+ transfer kinetics at low temperatures.[33,52] Despite the relatively higher surface diffusion energies, the Li−Ag alloy possesses a reasonably higher voltage than the lithium metal, which provides electrochemical driving forces to accelerate lithium ions transfer within the PAF layer.[7] We also theoretically investigated the chemical interaction between Li and LiF, LiAg, and PDOL components in the PAF. The Li_2CO_3 on a bare Li surface was also calculated for comparison. As displayed in Figure 4e and Figure S21, the adsorption energies of LiF, LiAg, and PDOL toward the Li atom are calculated to be −0.72, −0.39, and −0.69 eV, respectively, all of which are much larger in magnitude than the Li atom on Li_2CO_3 (−0.12 eV). The strong interplay between Li^+ and the PAF layer can tune the uniform distribution of Li ionic flux on the Li metal surface and offer massive Li^+ nucleation sites.

The advantages of the artificial PAF interphase over the electrolyte-derived Li_2CO_3-rich native SEI in regulating Li deposition behavior were further validated in a visualized clue by finite element simulation.[53−55] As depicted in Figure 4e and Figure S22, during galvanostatic deposition at a low temperature of −40 °C, a nonuniform Li^+ concentration can be observed above the vicinity of the pristine Li anode owing to the poor Li affinity and diffusivity of the native SEI. The intense concentration polarization is conducive to triggering the growth of Li dendrites (Figure S23a). After establishing the PAF interphase on the Li anode surface (Figure 4f), the concentration polarization region is significantly reduced, along with enriched Li^+ concentration in the whole electrode architecture. These simulation results indicate that Li^+ can accelerate and uniformly pass through the PAF-Li−electrolyte interface during low-temperature plating, accounting for dendrite-free Li deposition (Figure S23b and c).[14,56]

Low-Temperature PAF-Li Metal Performance in Symmetric Cells. According to the above discussion, the hybrid polymer-alloy-fluoride interphase in this contribution endows the Li metal anode with two intriguing features for low-temperature cycling (Figure 4): (1) The first is fast ion transport. The superior lithiophilicity of the polymer, alloy, and fluoride components in the PAF interphase enables preferential

https://doi.org/10.1021/acsnano.3c08576

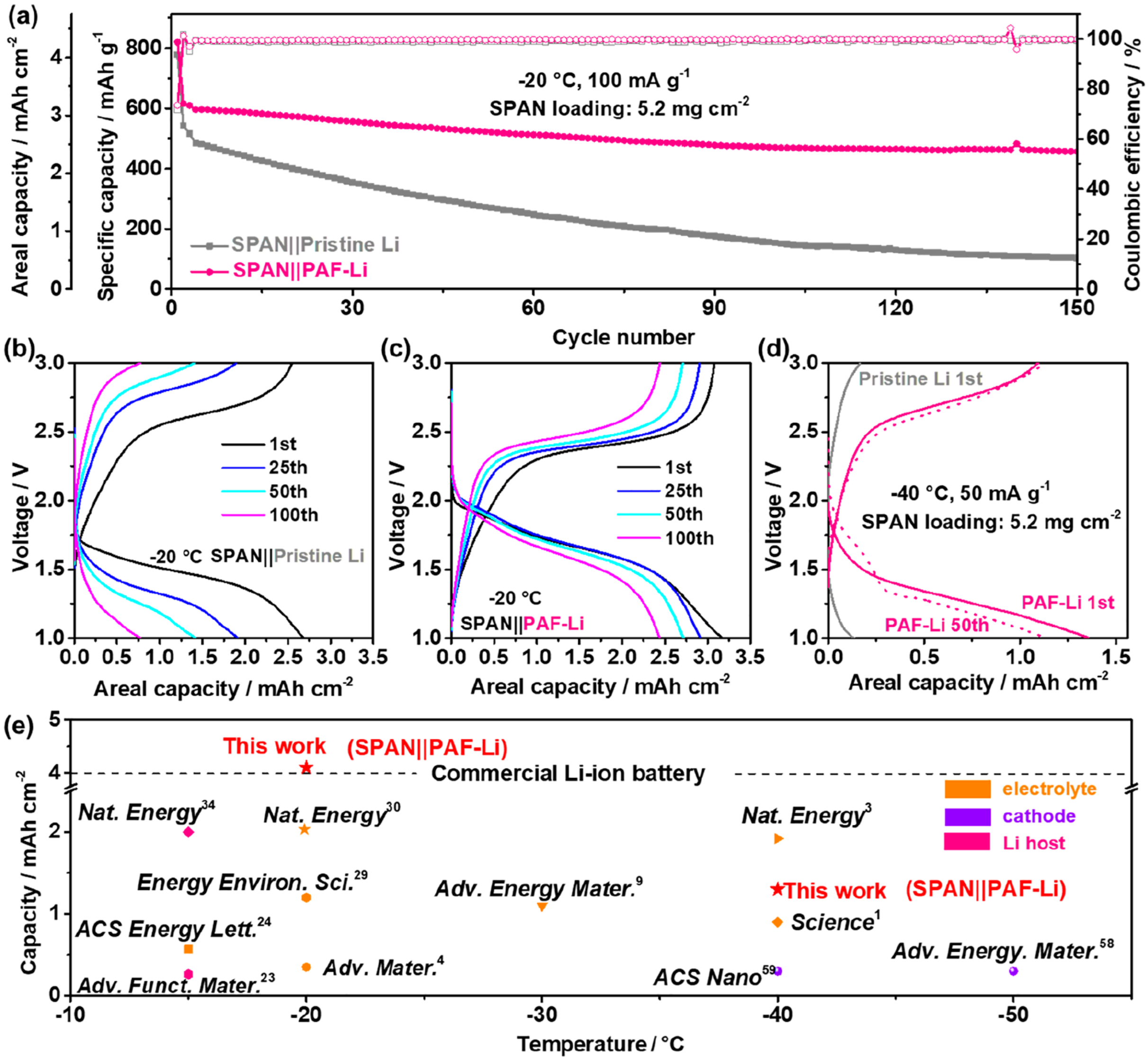

Figure 5. Electrochemical performance of PAF-Li electrodes in full cells. (a−d) Cycling performance of SPAN||pristine Li and SPAN||PAF-Li full cells and the corresponding charge/discharge voltage profiles at temperatures of (a−c) −20 °C and (d) at −40 °C. (e) Electrochemical performance comparison between our SPAN||PAF-Li cell and previously reported low-temperature lithium metal batteries. The related data are collected from Table S4.

absorption of Li$^+$ ions in the electrolyte and facilitated dissociation of Li$^+$ from the solvation sheath, assisting their desolvation at the electrolyte-electrode interface. In addition, the Li−Ag alloy with high lithium-ion diffusivity (∼10^{-8} cm^2 s^{-1} vs ∼10^{-11} cm^2 s^{-1} in bulk metal Li) expedites the Li transport within the PAF layer,[42,44] and the PDOL and LiF components serve as ionic pathways to reduce Li$^+$ diffusion barriers within the PAF layer. Therefore, the PAF layer effectively facilitates the two critical steps during the Li deposition process, namely, Li$^+$ desolvation and Li$^+$ diffusion through interphase on the electrode surface. (2) The second is strong electrode stability. Owing to the high chemical potential, Li−Ag alloy is conducive to reducing the reactivity of metallic Li with electrolyte solutions, thus effectively retarding electrolyte decomposition.[43] The synergistic soft-rigid feature of PDOL and LiF also endows the PAF hybrid layer with good shape conformability and dendrite-suppression effect. With a compact architecture, the designed PAF hybrid layer also effectively protects the underlying Li substrates from electrolyte corrosion, realizing superior suppression of Li dendrite growth and significant maintenance of electrode structural integrity during long-term low-temperature cycling.

Low-Temperature PAF-Li Metal Performance in Full Cells. In order to further evaluate the potential application of PAF-Li metal electrodes at low temperatures, sulfurized polyacrylonitrile (SPAN) cathodes with high capacity and good low-temperature tolerance were chosen as the basis of eventual full-cell configuration.[3] By coupling a high-loading (5.2 mg cm^{-2}) SPAN cathode with a PAF-Li metal anode (∼300 μm), the assembled full cell delivered a high initial areal capacity of 4.26 mAh cm^{-2} (819.2 mAh g^{-1}) at a current of 50 mA g^{-1} at −20 °C (Figures S24−S27). When cycled at 100 mA g^{-1} (Figure 5a), the initial discharge capacity of the SPAN||PAF-Li cell reached 3.17 mAh cm^{-2} (609.6 mAh g^{-1}) and the capacity remains at 2.37 mAh cm^{-2} (455.8 mAh g^{-1}) after 150 cycles, corresponding to 74.7% capacity retention. Meanwhile, the Coulombic efficiency calculated by averaging the CE from 150 cycles was found to be 99.6%. In comparison, the control cell using pristine Li anode experienced continuous capacity decay with a capacity retention of 19.1% (0.53 mAh cm^{-2}, 101.9 mAh g^{-1}) and a decreased average CE of 99.0% for 150 cycles. A rapid increase in voltage hysteresis of the SPAN||pristine Li cell with cycling could also be observed from the corresponding charging−discharging voltage curves (Figure 5b), which gave rise to a low energy efficiency of 45% after 150 cycles. Impressively, the full cell using a PAF-Li electrode displayed significantly reduced voltage hysteresis yet increased energy efficiency (~71%), which remained almost unchanged during long-term cycling (Figure 5c and Figure S28), demonstrating its strong interfacial stability and fast reaction kinetics. Such advantages also endow the SPAN||PAF-Li full cell with great improvements in both the initial capacity (2.17 mAh cm^{-2}) and prolonged lifespan (over 200 cycles) compared to the SPAN||pristine Li cell, which can only operate for several cycles at a large gravimetric current of 500 mA g^{-1} (Figure S29).

When the temperature further decreased to −40 °C (Figure 5d), the SPAN||pristine Li cell released a negligible capacity (~0.1 mAh cm^{-2}), which is related to the large voltage polarization and cell impedance. Notably, the SPAN cell with PAF-Li metal anode still delivered a high areal capacity of 1.36 mAh cm^{-2} (251.6 mAh g^{-1}), high capacity retention of 82.1%, and a high average CE of 99.0% for 50 cycles. The corresponding energy efficiency (Figure S30) remained at ~50% throughout the cycling at −40 °C, which are slightly lower than those of transition metal oxides (e.g., $LiFePO_4$, $LiCoO_2$; $LiNi_8Mn_1Co_1O_2$: $LiNi_{0.8}Co_{0.15}Al_{0.05}O_2$)-based Li metal full cell.[9,24,34] This phenomenon may be explained by the low electronic conductivity of SPAN cathode and its solid−solid conversion process.[3,57] The post-mortem SEM investigations (Figure S31) indicate that the PAF-Li maintains its structural integrity after cycling, in sharp contrast to the serious corrosion of the pristine Li electrode. These results strongly validate the significant role of the hybrid polymer-alloy-fluoride interphase in building advanced Li metal electrodes for practical high-energy-density LMBs at low temperatures.

From a historical perspective, we summarize the innovations and electrochemical performance of previously published low-temperature LMBs in Figure 5e and Table S4. One breakthrough low-temperature operation of Li metal batteries was proposed by Meng et al. in 2017 using a liquified gases electrolyte to enable sufficient ionic conductivities at −60 °C.[1] Inspired by this work, comprehensive low-temperature tolerant electrolytes have also been explored by using the all-fluoride electrolyte,[30,31] cosolvent electrolyte,[12,24,28,29] solvated electrolyte,[3,9] dilute electrolyte,[2] and colloid electrolyte.[4] Other research progress includes creating functional current collectors to host metallic Li[25,34] and constructing catalytic/amorphous cathodes to improve reaction dynamics.[58,59] However, these state-of-the-art low-temperature LMBs fail to reach the standard of commercial LIBs (~4 mAh cm^{-2}). The primary appeal of Li-metal anodes is their capability to realize higher energy densities than traditional anode materials. In this regard, our SPAN||PAF-Li battery is the prototype of a low-temperature lithium metal battery that delivers an industrial-level areal capacity (~4 mAh cm^{-2}). Such excellent performance suggests that constructing a hybrid polymer-alloy-fluoride interphase is a promising strategy to overcome kinetics and stability challenges in low-temperature Li-metal batteries. We also expect that our PAF-Li metal anode can synergize with other advanced electrolytes, nanostructured Li hosts, as well as innovative cathodes to further enhance the performance of Li-metal batteries under extremely low-temperature environments.

CONCLUSION

In summary, focusing on addressing inherent reaction kinetics and stability issues of low-temperature Li-metal batteries, we have successfully explored a facile design of a hybrid PAF interphase for the Li metal anode. Revealed by a combination of experimental characterizations and DFT computations, the PDOL, Li−Ag, and LiF components in the PAF hybrid interphase bring a synergistic effect of facilitating rapid electrochemical Li deposition reaction kinetics via reducing the energy barriers for Li^+ desolvation at the electrode−electrolyte interface and its diffusion on the electrode surface. The PAF hybrid interphase also exhibits multifunctional structural features with sufficient flexibility for maintaining the composite electrode integrity, excellent mechanical rigidity for restraining Li dendrite growth, and strong adhesion capability for avoiding undesired parasitic reactions with liquid electrolytes. Benefiting from these compositional and structural advantages, the as-designed PAF-Li electrode can work steadily for ~720 h with low voltage hysteresis and dendrite-free Li deposition behavior at a low temperature of −40 °C. Matched with high-loading cathodes, the assembled full cells exhibit unparalleled low-temperature performance in terms of high areal capacity (4.26 mAh cm^{-2}) and long cycling life (150 cycles) at −20 °C, as well as high capacity retention (82.1% after 50 cycles) at −40 °C. The above demonstration of hybrid polymer-alloy-fluoride interphase sheds fresh light on improving electrochemical reaction kinetics and stability at low temperatures, which affords an innovative approach toward realizing the targeted development of high-energy-density and all-weather energy storage and conversion systems.

EXPERIMENTAL SECTION

Preparation and PAF-Li Metal. 50 μL of 0.1 M $AgBF_4$ (99%, Adamas) in DOL (99.5%, Sigma-Aldrich) solution was dropped onto the lithium foil (12 mm in diameter, China Energy Lithium Co., Ltd.), and a hybrid PAF interphase was formed on the lithium foil after 3 min. Then, the Li foil was washed in a corresponding blank solvent to remove the residual impurities and then dried in an Ar-filled Mikrouna glovebox (H_2O < 0.1 ppm, O_2 < 0.1 ppm) at room temperature. The control sample was prepared by a similar process, just replacing the 0.1 M $AgBF_4$ in a DOL solution with 0.1 M $AgBF_4$ in a DME (99.5%, Sigma-Aldrich) solution or 0.1 M $LiBF_4$ (99%, Aladdin) in a DOL solution. The moisture content in the DOL and DME solvents is determined to be ~20 ppm using Karl Fischer Coulometer C30X (Mettler Toledo).

Materials Characterization. Scanning electron microscope (SEM) and energy dispersive X-ray spectrometry (EDX) mapping investigations were obtained on field emission SEM (Zeiss, Gemini 300) coupled with Oxford energy dispersive spectroscopy. FT-IR spectra were recorded on a Bruker Vertex 70 FTIR spectrometer. XRD patterns were recorded by X'Pert3 Powder (Malvern Panalytical. Co., Ltd.) using Cu Kα radiation at room temperature. X-ray photoelectron spectroscopy (XPS) was performed on an AXIS-ULTRA DLD-600W (SHIMADZU-KRATOS. Co., Ltd.). Ar-ion etching was carried out to remove the surface oxidation layer of the sample before the collection of XPS information. Time-of-flight secondary ion mass spectrometry (TOF-SIMS) was conducted using an ION-TOF (Gmhb 5, Münster, Germany) with an Ar-ion beam.

Electrochemical Analysis. Electrochemical measurements were carried out using CR2032 coin-type cells at room temperature. All cells were assembled in an Ar-filled Mikrouna glovebox (H_2O < 0.1 ppm, O_2 < 0.1 ppm), using Celgard 2400 as the separator, 1 M LiTFSI in DOL:DME:FEC (5:5:1, v/v) as the electrolytes with a certain amount of 40 μL, unless otherwise stated. The galvanostatic cycling measurements were performed on a Neware BTS-5 V battery tester (Shenzhen, China) at different current densities with different capacities. The linear sweep voltammetry (LSV) measurements were performed on a BioLogic VMP-300 workstation in the voltage range of −0.12 V to 0.12 V (vs Li^+/Li) with a scan rate of 0.1 mV s^{-1}. The Nyquist plots were collected on the above workstation in a frequency range from 500 kHz to 50 mHz under an amplitude of 10 mV. Li||Li symmetrical cells were assembled with two pristine Li and PAF-Li metal anodes. For the SPAN (sulfurized polyacrylonitrile)||Li full cells, SPAN was prepared according to the previous work[57] and used as the cathode. Element analysis results indicated that the weight of C, N, O, and S was 49.15%, 9.67%, 1.77%, and 39.41%, respectively. The SPAN cathode was made by blending SPAN power, Ketjen black, CNT, polyacrylic acid (PAA) with a weight ratio of 8:0.5:0.5:1 to form the slurry and then coated on the Al foil (10 mm in diameter). After drying at 80 °C under vacuum overnight, the obtained electrodes with areal mass loading controlled to be ~5.2 mg cm^{-2}. A thermal test chamber was used to carry out low-temperature tests. Before low-temperature tests, batteries were rested at low temperatures (−20 or −40 °C) for 1 h.

First-Principles Computation Details. All density functional theory (DFT) calculations[60,61] in this work were performed using CASTEP based on the on-the-fly-generated QC5 pseudopotentials,[62,63] and the generalized gradient approximation (GGA)[64] in the Perdew−Burke−Ernzerhof (PBE) functional[65] was implemented. An energy cutoff of 700 eV was set for the plane wave basis, and γ point-only was employed for the Brillouin zone. The chemical stability of the interface was evaluated by calculating the reaction energy based on the Materials Project (MP) database.[66] We carried out the nudged elastic band (NEB) method[67] to explore the diffusion mechanism of Li-ion in LiAg, LiF, Li_2CO_3, and PDOL.

ASSOCIATED CONTENT

Supporting Information

The Supporting Information is available free of charge at https://pubs.acs.org/doi/10.1021/acsnano.3c08576.

Additional SEM images, EDX mappings, digital photos, XRD patterns, XPS and IR spectra, electrochemical results (EIS, voltage/time curves, voltage/capacity curves, and cycling performance), and conclusion tables (PDF)

AUTHOR INFORMATION

Corresponding Author

Yongming Sun − *Wuhan National Laboratory for Optoelectronics, Huazhong University of Science and Technology, Wuhan, Hubei 430074, P. R. China;* orcid.org/0000-0001-8528-525X; Email: yongmingsun@hust.edu.cn

Authors

Yuanjian Li − *Wuhan National Laboratory for Optoelectronics, Huazhong University of Science and Technology, Wuhan, Hubei 430074, P. R. China; Institute of Materials Research and Engineering (IMRE), Agency for Science, Technology and Research (A*STAR), Singapore 138634, Republic of Singapore;* orcid.org/0000-0002-0356-3234

Eryang Mao − *Wuhan National Laboratory for Optoelectronics, Huazhong University of Science and Technology, Wuhan, Hubei 430074, P. R. China*

Zhiwen Min − *Shenzhen Institutes of Advanced Technology, Chinese Academy of Sciences, Shenzhen 518055, China*

Zhao Cai − *Wuhan National Laboratory for Optoelectronics, Huazhong University of Science and Technology, Wuhan, Hubei 430074, P. R. China;* orcid.org/0000-0001-7110-9300

Zihe Chen − *Wuhan National Laboratory for Optoelectronics, Huazhong University of Science and Technology, Wuhan, Hubei 430074, P. R. China*

Lin Fu − *Wuhan National Laboratory for Optoelectronics, Huazhong University of Science and Technology, Wuhan, Hubei 430074, P. R. China;* orcid.org/0000-0001-6834-2881

Xiangrui Duan − *Wuhan National Laboratory for Optoelectronics, Huazhong University of Science and Technology, Wuhan, Hubei 430074, P. R. China*

Lingyue Wang − *Wuhan National Laboratory for Optoelectronics, Huazhong University of Science and Technology, Wuhan, Hubei 430074, P. R. China*

Chang Zhang − *School of Physical Science and Technology, ShanghaiTech University, Shanghai 201210, China;* orcid.org/0000-0003-0404-2446

Ziheng Lu − *Shenzhen Institutes of Advanced Technology, Chinese Academy of Sciences, Shenzhen 518055, China*

Wei Liu − *School of Physical Science and Technology, ShanghaiTech University, Shanghai 201210, China;* orcid.org/0000-0002-6206-8321

Zhi Wei Seh − *Institute of Materials Research and Engineering (IMRE), Agency for Science, Technology and Research (A*STAR), Singapore 138634, Republic of Singapore;* orcid.org/0000-0003-0953-567X

Complete contact information is available at: https://pubs.acs.org/10.1021/acsnano.3c08576

Author Contributions

⊥Y.L., E.M., and Z.M. contributed equally.

Notes

The authors declare no competing financial interest.

ACKNOWLEDGMENTS

Y.S. acknowledges the financial support by the National Natural Science Foundation of China (Grants 52272207 and 52072137) and the Innovation Fund of Wuhan National Laboratory for Optoelectronics of Huazhong University of Science and Technology. Z.W.S. acknowledges the support of the Singapore National Research Foundation (Grant NRF-NRFF2017-04). The authors thank the Analytical and Testing Center of Huazhong University of Science and Technology as well as the Center for Nanoscale Characterization & Devices of Wuhan National Laboratory for Optoelectronics for providing the facilities to conduct the characterization.

REFERENCES

(1) Rustomji, C. S.; Yang, Y.; Kim, T. K.; Mac, J.; Kim, Y. J.; Caldwell, E.; Chung, H.; Meng, Y. S. Liquefied Gas Electrolytes for Electrochemical Energy Storage Devices. *Science* **2017**, *356*, 6345.

(2) Ji, H.; Wang, Z.; Sun, Y.; Zhou, Y.; Li, S.; Zhou, J.; Qian, T.; Yan, C. Weakening Li^+ De-solvation Barrier for Cryogenic Li-S Pouch Cells. *Adv. Mater.* **2023**, *35*, 2208590.

(3) Holoubek, J.; Liu, H.; Wu, Z.; Yin, Y.; Xing, X.; Cai, G.; Yu, S.; Zhou, H.; Pascal, T. A.; Chen, Z.; Liu, P. Tailoring Electrolyte Solvation for Li Metal Batteries Cycled at Ultra-Low Temperature. *Nat. Energy* **2021**, *6*, 303−313.

(4) Wang, X.; Yang, L.; Ahmad, N.; Ran, L.; Shao, R.; Yang, W. Colloid Electrolyte with Changed Li^+ Solvation Structure for High-Power, Low-Temperature Lithium-Ion Batteries. *Adv. Mater.* **2023**, *35*, 2209140.

(5) Yan, K.; Lu, Z.; Lee, H.-W.; Xiong, F.; Hsu, P.-C.; Li, Y.; Zhao, J.; Chu, S.; Cui, Y. Selective Deposition and Stable Encapsulation of Lithium through Heterogeneous Deeded Growth. *Nat. Energy* **2016**, *1*, 16010.

(6) Wang, X.; He, Y.; Liu, S.; Li, Y.; Tu, S.; Zhan, R.; Chen, Z.; Fu, J.; Cai, Z.; Wang, L.; Sun, Y. Dynamic Concentration of Alloying Element on Anode Surface Enabling Cycle-Stable Li Metal Batteries. *Adv. Funct. Mater.* **2023**, *33*, 2307281.

(7) Zhang, R.; Chen, X.; Shen, X.; Zhang, X.-Q.; Chen, X.-R.; Cheng, X.-B.; Yan, C.; Zhao, C.-Z.; Zhang, Q. Coralloid Carbon Fiber-Based Composite Lithium Anode for Robust Lithium Metal Batteries. *Joule* **2018**, *2*, 764−777.

(8) Zheng, X.; Cao, Z.; Luo, W.; Weng, S.; Zhang, X.; Wang, D.; Zhu, Z.; Du, H.; Wang, X.; Qie, L.; et al. Solvation and Interfacial Engineering Enable −40 °C Operation of Graphite/NCM Batteries at Energy Density over 270 wh kg^{-g}. *Adv. Mater.* **2023**, *35*, 2210115.

(9) Wang, Z.; Sun, Z.; Shi, Y.; Qi, F.; Gao, X.; Yang, H.; Cheng, H. M.; Li, F. Ion-Dipole Chemistry Drives Rapid Evolution of Li Ions Solvation Sheath in Low-Temperature Li Batteries. *Adv. Energy Mater.* **2021**, *11*, 2100935.

(10) Thenuwara, A. C.; Shetty, P. P.; Kondekar, N.; Sandoval, S. E.; Cavallaro, K.; May, R.; Yang, C.-T.; Marbella, L. E.; Qi, Y.; McDowell, M. T. Efficient Low-Temperature Cycling of Lithium Metal Anodes by Tailoring the Solid Electrolyte Interphase. *ACS Energy Lett.* **2020**, *5*, 2411−2420.

(11) Jin, C. B.; Yao, N.; Xiao, Y.; Xie, J.; Li, Z.; Chen, X.; Li, B. Q.; Zhang, X. Q.; Huang, J. Q.; Zhang, Q. Taming Solvent−Solute Interaction Accelerates Interfacial Kinetics in Low-Temperature Lithium-Metal Batteries. *Adv. Mater.* **2023**, *35*, 2208340.

(12) Dong, X.; Guo, Z.; Guo, Z.; Wang, Y.; Xia, Y. Organic Batteries Operated at −70 °C. *Joule* **2018**, *2*, 902−913.

(13) Duan, X.; Wang, L.; Li, G.; Liu, X.; Wan, M.; Du, J.; Zhan, R.; Wang, W.; Li, Y.; Tu, S.; et al. Revealing the Intrinsic Uneven Electrochemical Reactions of Li Metal Anode in Ah-Level Laminated Pouch Cells. *Adv. Funct. Mater.* **2023**, *33*, 2210669.

(14) Lu, G.; Nai, J.; Yuan, H.; Wang, J.; Zheng, J.; Ju, Z.; Jin, C.; Wang, Y.; Liu, T.; Liu, Y.; Tao, X. In-Situ Electrodeposition of Nanostructured Carbon Strengthened Interface for Stabilizing Lithium Metal Anode. *ACS Nano* **2022**, *16*, 9883−9893.

(15) Li, S.; Huang, J.; Cui, Y.; Liu, S.; Chen, Z.; Huang, W.; Li, C.; Liu, R.; Fu, R.; Wu, D. A Robust All-Organic Protective Layer Towards Ultrahigh-Rate and Large-Capacity Li Metal Anodes. *Nat. Nanotechnol.* **2022**, *17*, 613−621.

(16) Tu, H.; Li, L.; Wang, Z.; Wang, J.; Lin, H.; Wang, M.; Yan, C.; Liu, M. Tailoring Electrolyte Solvation for LiF-Rich Solid Electrolyte Interphase toward a Stable Li Anode. *ACS Nano* **2022**, *16*, 16898−16908.

(17) Han, B.; Xu, D.; Chi, S.-S.; He, D.; Zhang, Z.; Du, L.; Gu, M.; Wang, C.; Meng, H.; Xu, K.; et al. 500 Wh kg^{-1} Class Li Metal Battery Enabled by a Self-Organized Core-Shell Composite Anode. *Adv. Mater.* **2020**, *32*, 2004793.

(18) Ma, Q.; Yue, J.; Fan, M.; Tan, S. J.; Zhang, J.; Wang, W. P.; Liu, Y.; Tian, Y. F.; Xu, Q.; Yin, Y. X.; et al. Formulating the Electrolyte Towards High-Energy and Safe Rechargeable Lithium-Metal Batteries. *Angew. Chem., Int. Ed.* **2021**, *60*, 16554−16560.

(19) Hu, A.; Chen, W.; Du, X.; Hu, Y.; Lei, T.; Wang, H.; Xue, L.; Li, Y.; Sun, H.; Yan, Y.; et al. An Artificial Hybrid Interphase for an Ultrahigh-Rate and Practical Lithium Metal Anode. *Energy Environ. Sci.* **2021**, *14*, 4115−4124.

(20) Liu, Y.; Tao, X.; Wang, Y.; Jiang, C.; Ma, C.; Sheng, O.; Lu, G.; Lou, X. W. Self-assembled Monolayers Direct a LiF-rich Interphase toward Long-life Lithium Metal Batteries. *Science* **2022**, *375*, 739−745.

(21) Zhang, N.; Deng, T.; Zhang, S.; Wang, C.; Chen, L.; Wang, C.; Fan, X. Critical Review on Low-Temperature Li-Ion/Metal Batteries. *Adv. Mater.* **2022**, *34*, 2107899.

(22) Dong, X.; Wang, Y. G.; Xia, Y. Promoting Rechargeable Batteries Operated at Low Temperature. *Acc. Chem. Res.* **2021**, *54*, 3883−3894.

(23) Wang, J.; Yang, M.; Zou, G.; Liu, D.; Peng, Q. Lithiation MXene Derivative Skeletons for Wide-Temperature Lithium Metal Anodes. *Adv. Funct. Mater.* **2021**, *31*, 2101180.

(24) Xiao, P.; Luo, R.; Piao, Z.; Li, C.; Wang, J.; Yu, K.; Zhou, G.; Cheng, H.-M. High-Performance Lithium Metal Batteries with a Wide Operating Temperature Range in Carbonate Electrolyte by Manipulating Interfacial Chemistry. *ACS Energy Lett.* **2021**, *6*, 3170−3179.

(25) Fan, C. Y.; Xie, D.; Zhang, X. H.; Diao, W. Y.; Jiang, R.; Wu, X. L. Homogeneous Li^+ Flux Distribution Enables Highly Stable and Temperature-Tolerant Lithium Anode. *Adv. Functi. Mater.* **2021**, *31*, 2102158.

(26) Han, Y.; Jie, Y.; Huang, F.; Chen, Y.; Lei, Z.; Zhang, G.; Ren, X.; Qin, L.; Cao, R.; Jiao, S. Enabling Stable Lithium Metal Anode through Electrochemical Kinetics Manipulation. *Adv, Funct. Mater.* **2019**, *29*, 1904629.

(27) Fu, L.; Wang, X.; Wang, L.; Wan, M.; Li, Y.; Cai, Z.; Tan, Y.; Li, G.; Zhan, R.; Seh, Z. W.; Sun, Y. A Salt-in-Metal Anode: Stabilizing the Solid Electrolyte Interphase to Enable Prolonged Battery Cycling. *Adv. Funct. Mater.* **2021**, *31*, 2010602.

(28) Dong, X.; Lin, Y.; Li, P.; Ma, Y.; Huang, J.; Bin, D.; Wang, Y.; Qi, Y.; Xia, Y. High-Energy Rechargeable Metallic Lithium Battery at 70 °C Enabled by a Cosolvent Electrolyte. *Angew. Chem., Int. Ed.* **2019**, *58*, 5623−5627.

(29) Yang, Y.; Yin, Y.; Davies, D. M.; Zhang, M.; Mayer, M.; Zhang, Y.; Sablina, E. S.; Wang, S.; Lee, J. Z.; Borodin, O.; et al. Liquefied Gas Electrolytes for Wide-Temperature Lithium Metal Batteries. *Energy Environ. Sci.* **2020**, *13*, 2209−2219.

(30) Fan, X.; Ji, X.; Chen, L.; Chen, J.; Deng, T.; Han, F.; Yue, J.; Piao, N.; Wang, R.; Zhou, X.; et al. All-Temperature Batteries Enabled by Fluorinated Electrolytes with Non-Polar Solvents. *Nat. Energy* **2019**, *4*, 882−890.

(31) Holoubek, J.; Yu, M.; Yu, S.; Li, M.; Wu, Z.; Xia, D.; Bhaladhare, P.; Gonzalez, M. S.; Pascal, T. A.; Liu, P.; et al. An All-Fluorinated Ester Electrolyte for Stable High-Voltage Li Metal Batteries Capable of Ultra-Low-Temperature Operation. *ACS Energy Lett.* **2020**, *5*, 1438−1447.

(32) Zhang, D.; Zhu, D.; Guo, W.; Deng, C.; Xu, Q.; Li, H.; Min, Y. The Fluorine-Rich Electrolyte as an Interface Modifier to Stabilize Lithium Metal Battery at Ultra-Low Temperature. *Adv. Funct. Mater.* **2022**, *32*, 2112764.

(33) Yu, J.; Lin, X.; Liu, J.; Yu, J. T. T.; Robson, M. J.; Zhou, G.; Law, H. M.; Wang, H.; Tang, B. Z.; Ciucci, F. In Situ Fabricated Quasi-Solid Polymer Electrolyte for High-Energy-Density Lithium Metal Battery Capable of Subzero Operation. *Adv. Energy Mater.* **2022**, *12*, 2102932.

(34) Gao, Y.; Rojas, T.; Wang, K.; Liu, S.; Wang, D.; Chen, T.; Wang, H.; Ngo, A. T.; Wang, D. Low-Temperature and High-Rate-Charging Lithium Metal Batteries Enabled by An Electrochemically Active Monolayer-Regulated Interface. *Nat. Energy* **2020**, *5*, 534−542.

(35) Tan, L.; Lan, X.; Chen, J.; Zhang, H.; Hu, R.; Zhu, M. LiF-Induced Stable Solid Electrolyte Interphase for a Wide Temperature SnO_2-Based Anode Extensible to −50 °C. *Adv. Energy Mater.* **2021**, *11*, 2101855.

(36) Li, G.; Duan, X.; Liu, X.; Zhan, R.; Wang, X.; Du, J.; Chen, Z.; Li, Y.; Cai, Z.; Shen, Y.; Sun, Y. Locking Active Li Metal through Localized Redistribution of Fluoride Enabling Stable Li-Metal Batteries. *Adv. Mater.* **2023**, *35*, 2207310.

(37) Yan, C.; Cheng, X.-B.; Yao, Y.-X.; Shen, X.; Li, B.-Q.; Li, W.-J.; Zhang, R.; Huang, J.-Q.; Li, H.; Zhang, Q. An Armored Mixed Conductor Interphase on a Dendrite-Free Lithium-Metal Anode. *Adv. Mater.* **2018**, *30*, 1804461.

(38) Pathak, R.; Chen, K.; Gurung, A.; Reza, K. M.; Bahrami, B.; Pokharel, J.; Baniya, A.; He, W.; Wu, F.; Zhou, Y.; et al. Fluorinated Hybrid Solid-Electrolyte-Interphase for Dendrite-Free Lithium Deposition. *Nat. Commun.* **2020**, *11*, 5429.

(39) Zhang, S.; Li, R.; Hu, N.; Deng, T.; Weng, S.; Wu, Z.; Lu, D.; Zhang, H.; Zhang, J.; Wang, X.; et al. Tackling Realistic Li^+ Flux for High-Energy Lithium Metal Batteries. *Nat. Commun.* **2022**, *13*, 5431.

(40) Wu, D.; He, J.; Liu, J.; Wu, M.; Qi, S.; Wang, H.; Huang, J.; Li, F.; Tang, D.; Ma, J. Li_2CO_3/LiF-Rich Heterostructured Solid Electrolyte Interphase with Superior Lithiophilic and Li^+-Transferred Characteristics via Adjusting Electrolyte Additives. *Adv. Energy Mater.* **2022**, *12*, 2200337.

(41) Liu, J.; Yuan, B.; He, N.; Dong, L.; Chen, D.; Zhong, S.; Ji, Y.; Han, J.; Yang, C.; Liu, Y.; et al. Reconstruction of LiF-Rich Interphases Through An Anti-Freezing Electrolyte for Ultralow-Temperature $LiCoO_2$ Batteries. *Energy Environ. Sci.* **2023**, *16*, 1024−1034.

(42) Zhang, S.; Yang, G.; Liu, Z.; Weng, S.; Li, X.; Wang, X.; Gao, Y.; Wang, Z.; Chen, L. Phase Diagram Determined Lithium Plating/Stripping Behaviors on Lithiophilic Substrates. *ACS Energy Lett.* **2021**, *6*, 4118−4126.

(43) Wu, X.; Zhang, W.; Wu, N.; Pang, S. S.; Ding, Y.; He, G. Structural Evolution upon Delithiation/Lithiation in Prelithiated Foil Anodes: A Case Study of AgLi Alloys with High Li Utilization and Marginal Volume Variation. *Adv. Energy Mater.* **2021**, *11*, 2003082.

(44) Jin, S.; Ye, Y.; Niu, Y.; Xu, Y.; Jin, H.; Wang, J.; Sun, Z.; Cao, A.; Wu, X.; Luo, Y.; Ji, H.; Wan, L. J. Solid−Solution-Based Metal Alloy Phase for Highly Reversible Lithium Metal Anode. Solid-solution-based metal alloy phase for highly reversible lithium metal anode. *J. Am. Chem. Soc.* **2020**, *142*, 8818−8826.

(45) Yang, H.; Zhang, B.; Jing, M.; Shen, X.; Wang, L.; Xu, H.; Yan, X.; He, X. In Situ Catalytic Polymerization of a Highly Homogeneous PDOL Composite Electrolyte for Long-Cycle High-Voltage Solid-State Lithium Batteries. *Adv. Energy Mater.* **2022**, *12*, 2201762.

(46) Liu, F.; Li, T.; Yang, Y.; Yan, J.; Li, N.; Xue, J.; Huo, H.; Zhou, J.; Li, L. Investigation on the Copolymer Electrolyte of Poly(1,3-dioxolane-co-formaldehyde). *Macromol. Rapid Commun.* **2020**, *41*, No. e2000047.

(47) Wang, W. P.; Zhang, J.; Yin, Y. X.; Duan, H.; Chou, J.; Li, S. Y.; Yan, M.; Xin, S.; Guo, Y. G. A Rational Reconfiguration of Electrolyte for High-Energy and Long-Life Lithium−Chalcogen Batteries. *Adv. Mater.* **2020**, *32*, 2000302.

(48) Zhao, Q.; Liu, X.; Stalin, S.; Khan, K.; Archer, L. A. Solid-State Polymer Electrolytes with In-Built Fast Interfacial Transport for Secondary Lithium Batteries. *Nat. Energy* **2019**, *4*, 365−373.

(49) Pu, J.; Li, J.; Zhang, K.; Zhang, T.; Li, C.; Ma, H.; Zhu, J.; Braun, P. V.; Lu, J.; Zhang, H. Conductivity and Lithiophilicity Gradients Guide Lithium Deposition to Mitigate Short Circuits. *Nat. Commun.* **2019**, *10*, 1896.

(50) Zheng, X.; Huang, L.; Luo, W.; Wang, H.; Dai, Y.; Liu, X.; Wang, Z.; Zheng, H.; Huang, Y. Tailoring Electrolyte Solvation Chemistry toward an Inorganic-Rich Solid-Electrolyte Interphase at a Li Metal Anode. *ACS Energy Lett.* **2021**, *6*, 2054−2063.

(51) Zheng, X.; Gu, Z.; Fu, J.; Wang, H.; Ye, X.; Huang, L.; Liu, X.; Wu, X.; Luo, W.; Huang, Y. Knocking Down the Kinetic Barriers towards Fast-Charging and Low-Temperature Sodium Metal Batteries. *Energy Environ. Sci.* **2021**, *14*, 4936−4947.

(52) Zhou, J.; Ji, H.; Qian, Y.; Liu, J.; Yan, T.; Yan, C.; Qian, T. Molecular Simulations Guided Polymer Electrolyte towards Superior Low-Temperature Solid Lithium-Metal Batteries. *ACS Appl. Mater. Interfaces* **2021**, *13*, 48810−48817.

(53) Yang, G.; Li, Y.; Zhang, C.; Wang, J.; Bai, Y.; Lim, C. Y. J.; Ng, M. F.; Chang, Z.; Kumar, S.; Sofer, Z.; Liu, W.; Seh, Z. W. In Situ Formed Magnesiophilic Sites Guiding Uniform Deposition for Stable Magnesium Metal Anodes. *Nano Lett.* **2022**, *22*, 9138−9146.

(54) Li, Y.; Yang, G.; Zhang, C.; Lieu, W. Y.; Lim, C. Y. J.; Sun, S.; Wang, J.; Jiang, S.; Xing, Z.; Sofer, Z.; et al. Grain-Boundary-Rich Triphasic Artificial Hybrid Interphase Toward Practical Magnesium Metal Anodes. *Adv. Funct. Mater.* **2023**, *33*, 2210639.

(55) Liao, Y.; Yuan, L.; Liu, X.; Meng, J.; Zhang, W.; Li, Z.; Huang, Y. Low-Cost Fumed Silicon Dioxide Uniform Li^+ Flux for Lean-Electrolyte and Anode-Free Li/S Battery. *Energy Storage Mater.* **2022**, *48*, 366−374.

(56) Wang, D.; Lv, D.; Liu, H.; Yang, J.; Qian, Y.; Chen, Z. Forming Solid-Electrolyte Interphases with Rich Grain Boundaries on 3D Lithiophilic Skeleton for Low-Temperature Lithium Metal Batteries. *Energy Storage Mater.* **2022**, *49*, 454−462.

(57) Chen, X.; Peng, L.; Wang, L.; Yang, J.; Hao, Z.; Xiang, J.; Yuan, K.; Huang, Y.; Shan, B.; Yuan, L.; Xie, J. Ether-Compatible Sulfurized Polyacrylonitrile Cathode with Excellent Performance Enabled by Fast Kinetics via Selenium Doping. *Nat. Commun.* **2019**, *10*, 1021.

(58) Yu, Z.; Wang, B.; Liao, X.; Zhao, K.; Yang, Z.; Xia, F.; Sun, C.; Wang, Z.; Fan, C.; Zhang, J.; Wang, Y. Boosting Polysulfide Redox Kinetics by Graphene-Supported Ni Nanoparticles with Carbon Coating. *Adv. Energy Mater.* **2020**, *10*, 2000907.

(59) Wang, Z.; Ji, H.; Zhou, L.; Shen, X.; Gao, L.; Liu, J.; Yang, T.; Qian, T.; Yan, C. All-Liquid-Phase Reaction Mechanism Enabling Cryogenic Li-S Batteries. *ACS Nano* **2021**, *15*, 13847−13856.

(60) Kohn, W.; Sham, L. Self-Consistent Equations Including Exchange and Correlation Effects. *Phys. Rev.* **1965**, *140*, A1133−A1138.

(61) Segall, M. D.; Lindan, P. J. D.; Probert, M. J.; Pickard, C. J.; Hasnip, P. J.; Clark, S. J.; Payne, M. C. First-Principles Simulation: Ideas, Illustrations and the CASTEP Code. *J. Phys.: Condens. Matter* **2002**, *14*, 2717.

(62) Lu, Z. Computational discovery of energy materials in the era of big data and machine learning: A critical review. *Mater. Rep. Energy* **2021**, *1*, 100047.

(63) Lu, Z.; Zhu, B.; Shires, W. B. B.; Scanlon, D. O.; Pickard, C. J. Ab initio random structure searching for battery cathode materials. *J. Chem. Phys.* **2021**, *154*, 174111.

(64) Blöchl, P. E. Projector augmented-wave method. *Phys. Rev. B* **1994**, *50*, 17953−17979.

(65) Perdew, J. P.; Burke, K.; Ernzerhof, M. Generalized Gradient Approximation Made Simple. *Phys. Rev. Lett.* **1996**, *77*, 3865−3868.

(66) Jain, A.; Ong, S. P.; Hautier, G.; Chen, W.; Richards, W. D.; Dacek, S.; Cholia, S.; Gunter, D.; Skinner, D.; Ceder, G.; Persson, K. A. Commentary: The Materials Project: A materials genome approach to accelerating materials innovation. *APL Mater.* **2013**, *1*, 170901.

(67) Henkelman, G.; Uberuaga, B. P.; Jónsson, H. J. A Climbing Image Nudged Elastic Band Method for Finding Saddle Points and Minimum Energy Paths. *J. Chem. Phys.* **2000**, *113*, 9901−9904.